*J. Fluid Mech.* (1983), *vol.* 132, *pp.* 209–230
*Printed in Great Britain*



# Transition of Taylor–Görtler vortex flow in spherical Couette flow

By KOICHI NAKABAYASHI
Department of Mechanical Engineering, Nagoya Institute of Technology, Japan

(Received 30 November 1982)

The critical Taylor number, phenomena accompanying the transition to turbulence, and the cellular structure of Taylor–Görtler vortex in the flow between two concentric spheres, of which the inner one is rotating and the outer is stationary, are investigated using three kinds of flow-visualization technique. The critical Taylor number generally increases with the ratio $\beta$ of clearance to inner-sphere radius. For $\beta \leqslant 0.08$, the critical Taylor number in spherical Couette flow is smaller than in circular Couette flow, but vice versa for $\beta > 0.08$. A pair of toroidal Taylor–Görtler vortices occurs first around the equator at the critical Reynolds number $R_{ec}$ (or critical Taylor number $T_c$). More Taylor–Görtler vortices are added with increasing Reynolds number $R_e$. After reaching the maximum number of vortex cells, as $R_e$ is increased, the number of vortex cells decreases along with the various transition phenomena of Taylor–Görtler vortex flow, and the vortex finally disappears for very large $R_e$, where the turbulent basic flow is developed. The instability mode of Taylor–Görtler vortex flow depends on both $\beta$ and $R_e$. The vortex flows encountered as $R_e$ is increased are toroidal, spiral, wavy, oscillating (quasiperiodic), chaotic and turbulent Taylor–Görtler vortex flows. Fourteen different flow regimes can be observed through the transition from the laminar basic flow to the turbulent basic flow. The number of toroidal and/or spiral cells and the location of toroidal and spiral cells are discussed as a means to clarify the spatial organization of the vortex. Toroidal cells are stationary. However, spiral cells move in relation to the rotating inner sphere, but in the reverse direction of its rotation and at about half its speed. The spiral vortices number about six, and the spiral angle is 2–10°.

## 1. Introduction

The flow between two concentric rotating spheres with the inner one rotating and the outer one stationary has been investigated theoretically and experimentally by many researchers. Below the critical Reynolds number, the laminar basic flow is a steady axisymmetric spiral flow superposing motion in circles and secondary motion between the equator and the pole driven by centrifugal force due to the rotation of the inner sphere. The flow characteristics above the critical Reynolds number depend greatly on the ratio $\beta$ of the clearance to the inner sphere radius. For the case of small $\beta$, the flow condition near the equator is so similar to the flow between two concentric rotating cylinders that Taylor instability occurs. For the case of large $\beta$, however, Munson & Menguturk (1975) and Waked & Munson (1978) reported that the laminar basic flow becomes unstable, not by means of Taylor instability, but by transforming directly into turbulent flow.

Taylor instability for the rotating spheres has been experimentally investigated by Khlebutin (1968), Yakushin (1970), Sawatzki & Zierep (1970), Munson &

| No. | Radius $R_1$ of inner sphere (mm) | Clearance $s$ (mm) | Clearance ratio $\beta$ | Critical Reynolds number $R_{ec}$ | Critical Taylor number $T_c$ |
|---|---|---|---|---|---|
| 1 | 85.49 ± 0.01 | 2.04 | 0.024 | 10700 | 39.4 |
| 2 | 82.55 ± 0.03 | 4.98 | 0.060 | 2760 | 40.6 |
| 3 | 76.89 ± 0.02 | 10.64 | 0.138 | 900 | 46.3 |
| 4 | 72.57 ± 0.01 | 14.96 | 0.206 | 554 | 51.3 |

TABLE 1. Dimensions of inner sphere, critical Reynolds and Taylor numbers

Menguturk (1975), Wimmer (1976), Nakabayashi (1978) and Yavorskaya *et al.* (1980). These experiments were done by torque measurements or flow-visualization techniques. Different modes of instability or Taylor–Görtler vortices were observed by Sawatzki & Zierep (1970) and Wimmer (1976), using aluminium flakes suspended in the working fluid. Wimmer classified the flow modes from I to V and discussed the relation between each flow mode and the coefficient of viscous frictional torque, as well as the relationship between wavelength and $R_e$ for $\beta = 0.18$. But no detailed results have been reported for other $\beta$-values, nor has the cellular structure of Taylor–Görtler vortices been clarified in sufficient detail.

In this study, the relationship between critical Taylor number $T_c$ and $\beta$, various transition phenomena of Taylor–Görtler vortex flow, and the cellular structure of toroidal and spiral Taylor–Görtler vortices are investigated for a wide range of $R_e$, using three different kinds of flow-visualization technique. For these experiments, $R_e$ was increased stepwise by increasing the angular velocity of the inner sphere, where the final flow field of the last step was used for the initial condition. The step sizes were so small that the final flow field obtained at a certain $R_e$ gave a simulation of an initial-value problem with an arbitrary small angular acceleration. For all that, only a certain selection out of all possible stable flow modes due to a definite $R_e$ could be made.

## 2. Experimental apparatus and flow-visualization techniques

The experimental apparatus is illustrated in figure 1. A stationary outer sphere was composed of two transparent acrylic plastic blocks, (1) and (2), having an inner spherical surface with the spherical radius $R_2 = 87.53 \pm 0.01$ mm. An inner aluminium alloy sphere (3) having the various radii $R_1$, shown in table 1, was installed with an accuracy of $\pm 0.02$ mm concentricity in the outer-sphere blocks (1) and (2). The inner sphere was rotated through a drive shaft (4) with a variable-speed motor by means of a pulley (5), and the revolutions were counted by a digital tachometer and a magnetic pick-up (6), using a rotary detection gear (7). Whip of the rotating inner sphere was assured to be within $\pm 0.01$–$0.03$ mm. Water and glycerol–water solutions of 50 % and 66 % concentrations were used for working fluids. The temperature was measured by a thermosensor (8).

Flow was observed by the surface oil-flow method and the aluminium-flake method. The surface oil-flow method was used to obtain streak patterns of Taylor–Görtler vortices and secondary flow on the inner and outer surfaces of the outer and inner spheres respectively. A mixture of titanium dioxide, diesel oil and oleic acid was used for the oil sheet. The oil sheet was so thin that its effect on the original fluid flow could be ignored. In addition to the front lighting of the whole flow region, the

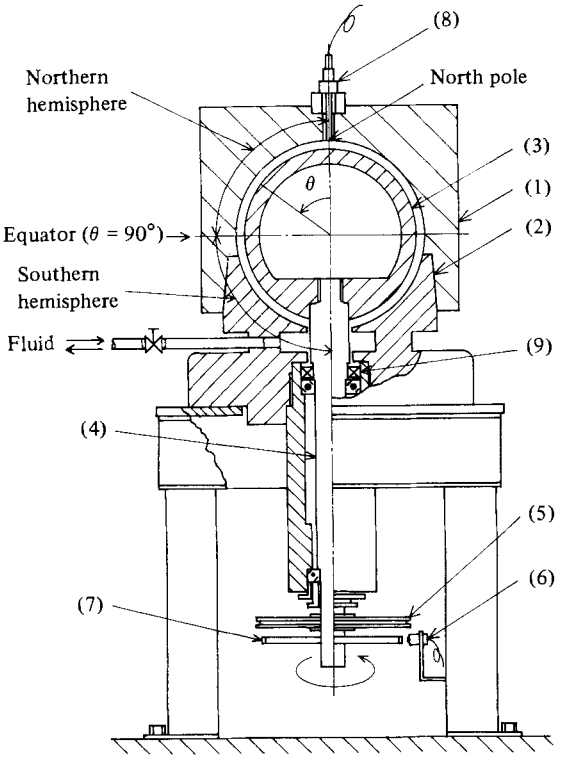


FIGURE 1. Experimental apparatus: (1), (2) Acrylite outer-sphere blocks; (3) rotating inner spheres; (4) drive shaft; (5) pulley; (6) magnetic pick-up; (7) rotary detection gear; (8) thermosensor; (9) oil seal.

aluminium-flake method was also employed to observe the meridional cross-section of the spherical annulus by slit illumination. By the abovementioned three visualization techniques, a remarkable image of the cellular structure of Taylor–Görtler vortex flow in spherical Couette flow could be obtained. Spherical coordinates $(r, \theta, \phi)$ were used, where $\theta$ is shown in figure 1. The measurements of the meridian coordinate $\theta$ of sinks and/or sources of Taylor–Görtler vortex cells observed on the inner sphere in a meridian cross-section of the spherical annulus were made by a cathetometer or from photographs, where only slit illumination was available. The position results $\theta$ (which are shown in figures 9 and 11) were corrected for optical distortion by the refraction errors measured in advance. The present experiment was done for four clearance ratios $\beta = 0.024$–$0.206$, which are shown in table 1. $\beta$ is defined by $\beta = s/R_1$, where $s$ is the clearance between inner and outer spheres.

## 3. Critical Taylor number

The instability of spherical Couette flow with a rotating inner sphere and a stationary outer one has not been sufficiently investigated either theoretically or experimentally. For the case of small $\beta$ (e.g. $\beta < 0.3$), Taylor instability occurs with the appearance of a pair of toroidal Taylor–Görtler vortices around the equator at the critical Reynolds number $R_{ec}$. The Reynolds number $R_e$ is defined by $R_e = R_1^2\,\omega_1/\nu$, where $R_1$ is the outer radius of the inner sphere, $R_2$ is the inner radius of the outer sphere, $s = R_2 - R_1$ is the clearance between the spheres, $\omega_1$ is the angular

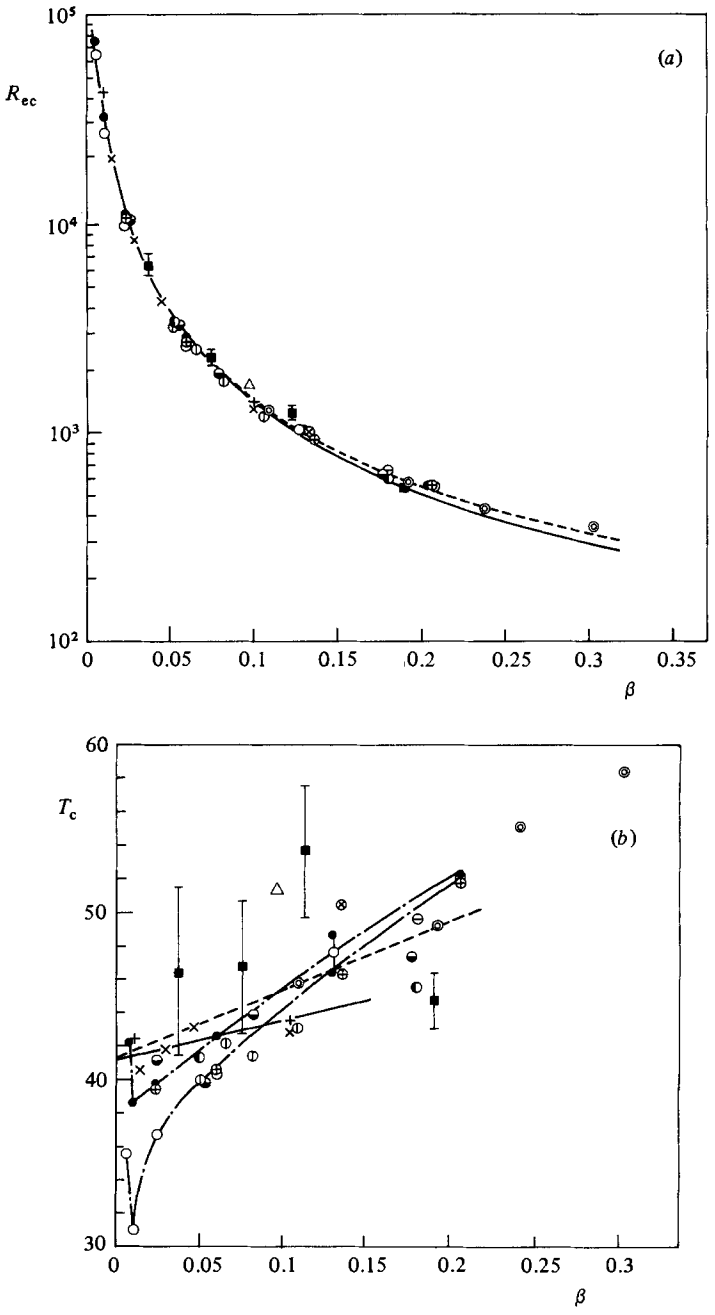


FIGURE 2. (*a*) Critical Reynolds number $R_{ec}$ as a function of ratio $\beta$ of clearance to inner-sphere radius. (*b*) Critical Taylor number $T_c$ as a function of $\beta$. Flow vizualization: ⊕, present data; ○, NAKABAYASHI (1978); ⊖, Wimmer (1976); ⦶, Sawatzki & Zierep (1970); ◎, Yavorskaya *et al.* (1980). Torque measurements: ■, Khlebutin (1968); △, Yakushin (1970); ⊗, Munson & Menguturk (1975); ◐, Sawatzki & Zierep (1970); ◒, Wimmer (1976); ●, Nakabayashi (1978); ----, Yavorskaya *et al.* (1980); —·—, Nakabayashi (1978). Torque measurements for two concentric rotating cylinders: +, Vohr (1968); ×, Nakabayashi *et al.* (1972), ——, Taylor (1923).

| Flow regime | Characteristics |
|---|---|
| I B | Laminar flow + secondary flow (laminar basic flow) |
| II T | Laminar flow + toroidal TG vortex + secondary flow |
| II TS | Laminar flow + toroidal and spiral TG vortex + secondary flow |
| II S | Laminar flow + spiral TG vortex + secondary flow |
| II TSt | Laminar flow + toroidal TG vortex + secondary flow with Stuart vortex |
| III WTS | Laminar flow + wavy toroidal and spiral TG vortex + secondary flow |
| III WS | Laminar flow + wavy spiral TG vortex + secondary flow |
| III WT | Laminar flow + wavy toroidal TG vortex + secondary flow |
| III T | Laminar flow + toroidal TG vortex with strong circulation + secondary flow |
| III OTSt | Laminar flow + oscillating toroidal TG vortex + secondary flow with Stuart vortex |
| IV S | Turbulent (chaotic) flow + spiral TG vortex + secondary flow |
| IV T | Turbulent flow + toroidal TG vortex + secondary flow |
| IV TSt | Turbulent flow + toroidal TG vortex + secondary flow with Stuart vortex |
| IV B | Turbulent flow + secondary flow (turbulent basic flow) |

TABLE 2. Characteristics of various flow regimes

velocity of the inner sphere and $\nu$ is the kinematic viscosity of working fluid. For the case of large $\beta$, $\beta > 0.3$, no occurrence of Taylor instability is reported by Munson & Menguturk (1975) or Waked & Munson (1978).

Here the critical Reynolds or Taylor number is discussed in relation to Taylor instability for small $\beta$. Figure 2(*a*) shows the critical Reynolds number $R_{ec}$ as a function of $\beta$ in comparison with the theoretical and experimental results for circular Couette flow. These experimental results were obtained by means of flow-visualization techniques or torque measurements. Sawatzki & Zierep (1970) and Wimmer (1976) concluded that the relationship between $R_{ec}$ and $\beta$ for spherical Couette flow is the same as for circular Couette flow. This conclusion seems to be correct when $\beta$ is extremely small, because the data are in good agreement with the theoretical and experimental results for circular Couette flow, as shown in figure 2(*a*). On the other hand, Yavorskaya *et al.* (1980) concluded that $R_{ec}$ for spherical Couette flow is greater than for circular Couette flow, and that the relationship between $R_{ec}$ and $\beta$ is given by

$$R_{ec} = 41.3(1+c\beta)\beta^{-\frac{1}{2}}, \quad \text{or} \quad T_c = 41.3(1+c\beta), \tag{1}$$

where $c \approx 1$ and the critical Taylor number $T_c$ is defined by $T_c = R_{ec}\beta^{\frac{3}{2}}$. Khlebutin (1968) also gives the following expression for $\beta \leqslant 0.12$:

$$R_{ec} = 49\beta^{-\frac{1}{2}}. \tag{2}$$

When $\log R_{ec}$ is plotted *vs.* $\beta$, $R_{ec}$ for spherical Couette flow seems to be in good agreement with that for circular Couette flow when $\beta \leqslant 0.08$, as shown in figure 2(*a*). If $T_c$ is considered as a function of $\beta$, however, as is shown in figure 2(*b*), the discrepancy between spherical and circular Couette flows is clear even for $\beta \leqslant 0.08$, as previously indicated by Nakabayashi (1978). Although the data vary greatly with the researcher, the single-dot lines obtained by the author give the most appropriate relationship between $T_c$ and $\beta$ for both torque measurements and flow-visualization results respectively.

The present results of $R_{ec}$ or $T_c$, which were obtained by the aluminium-flake method with both the front lighting and slit illumination, agreed with the previous results with one exception. For $\beta = 0.024$, $R_{ec} = 10700$ was obtained by slit

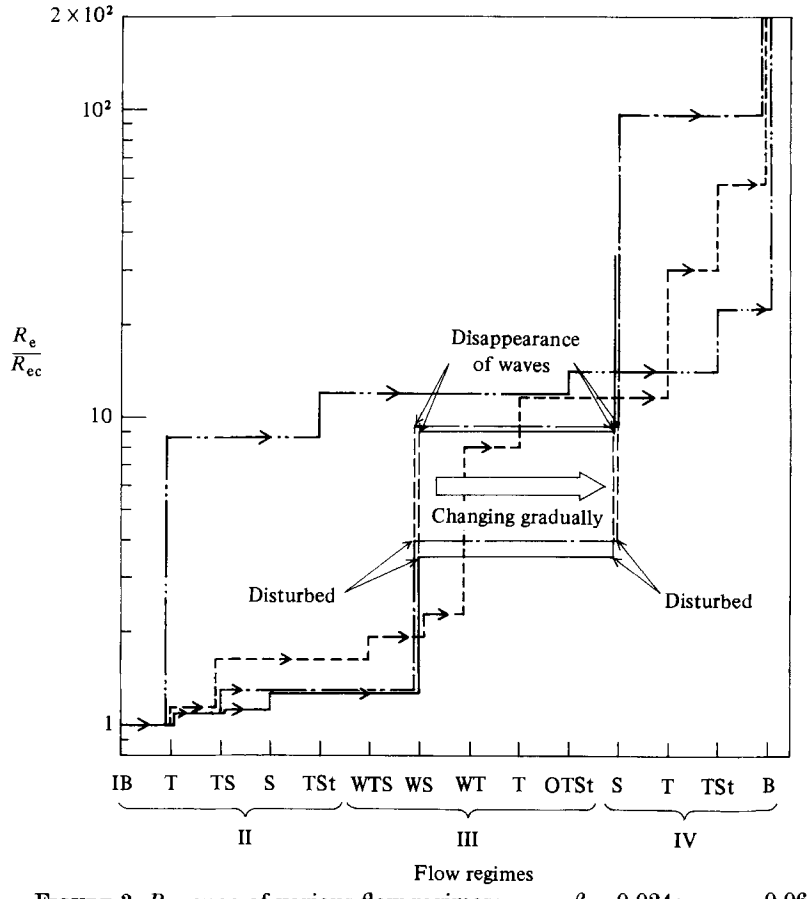


FIGURE 3. *Re*-range of various flow regimes: ——, $\beta = 0.024$; —·—, 0.06; – – – –, 0.138; —··—, 0.206.

illumination, as shown in table 1, but $R_{ec} = 9900$ was obtained by front lighting in the same experiment. This discrepancy was caused by the fact that no cell of Taylor–Görtler vortex (hereinafter TG vortex) could be clearly observed by slit illumination below $R_e = 10700$, although the TG vortex could be clearly observed by front lighting above $R_e = 9900$. Therefore $R_{ec} = 9900$ was considered to give the onset of the formation of the Taylor–Görtler vortex. However, no discrepancy from use of these two illumination techniques resulted for any other $\beta$.

The following conclusion can be derived as to Taylor instability for spherical Couette flow. The value of $T_c$ for the spherical Couette flow is smaller than for the circular Couette flow for $\beta \leqslant 0.08$. For $\beta > 0.08$, however, $T_c$ for the former is greater than for the latter. As $\beta$ approaches 0, both reach asymptotically the same value (about 41.3). Hence it is reasonable to expect that the $T_c$ tendency described above will be caused by the Ekman boundary-layer effect, which acts on the unstable side for $\beta < 0.08$, and on the stable side for $\beta > 0.08$.

## 4. Instability and transition phenomena

When the Reynolds number $R_e$ increases gradually, the fourteen flow regimes which are summarized in table 2 can be observed through various transition processes from

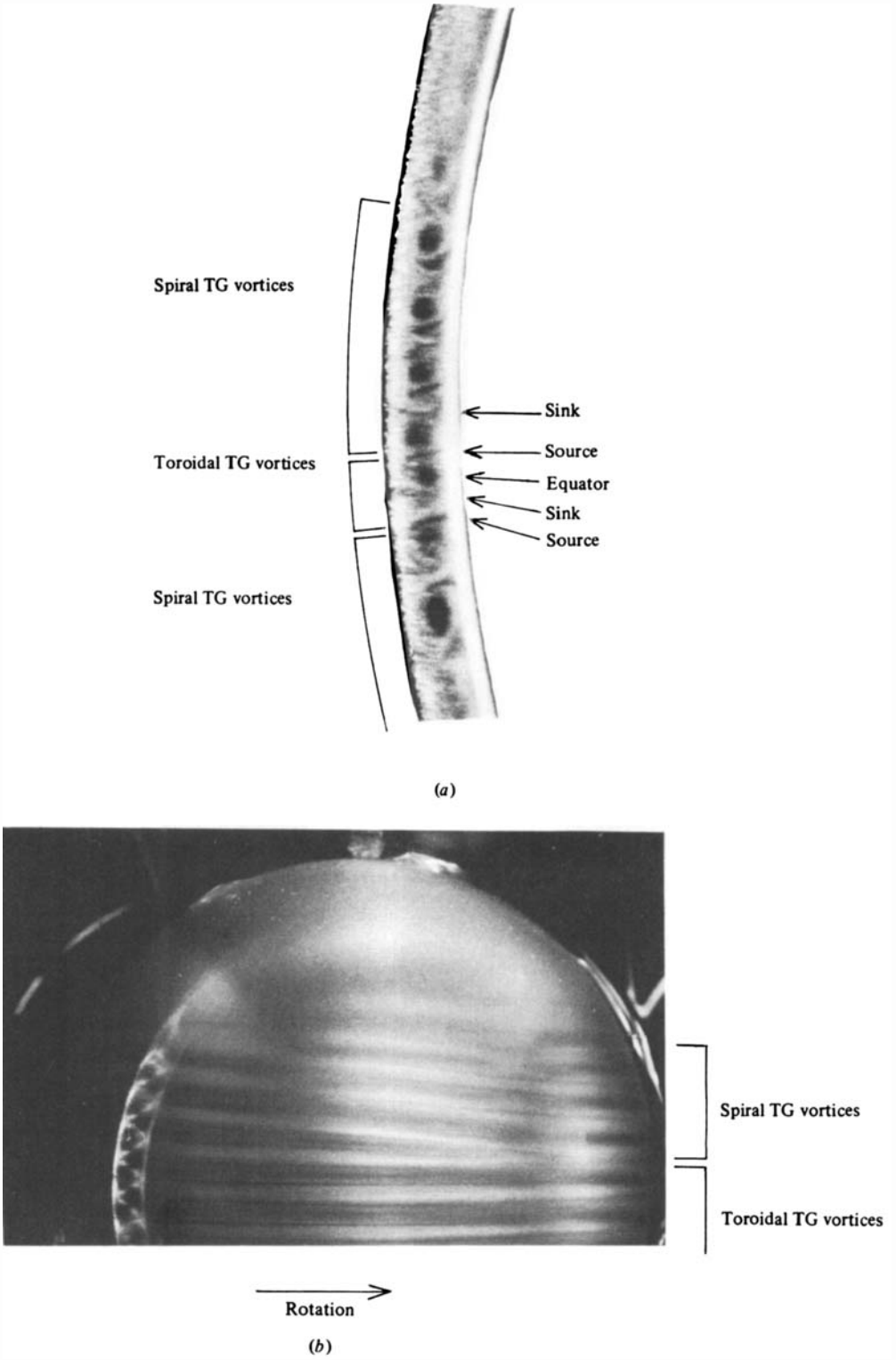


FIGURE 4(*a*, *b*). For caption see p. 217.

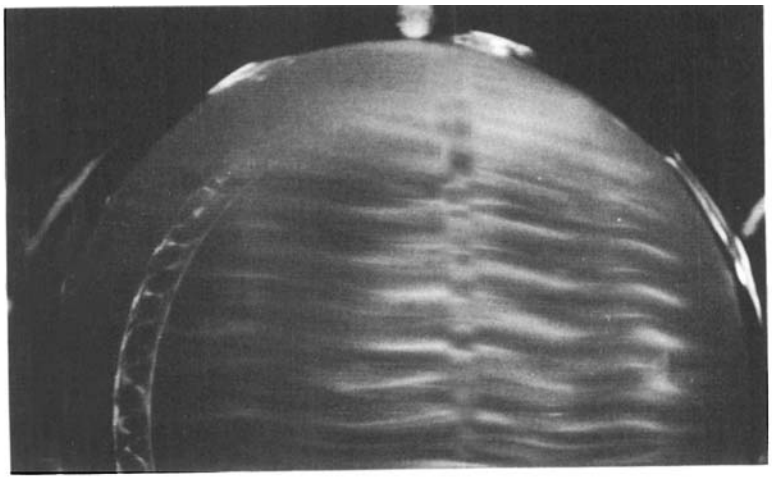

Rotation

(*c*)

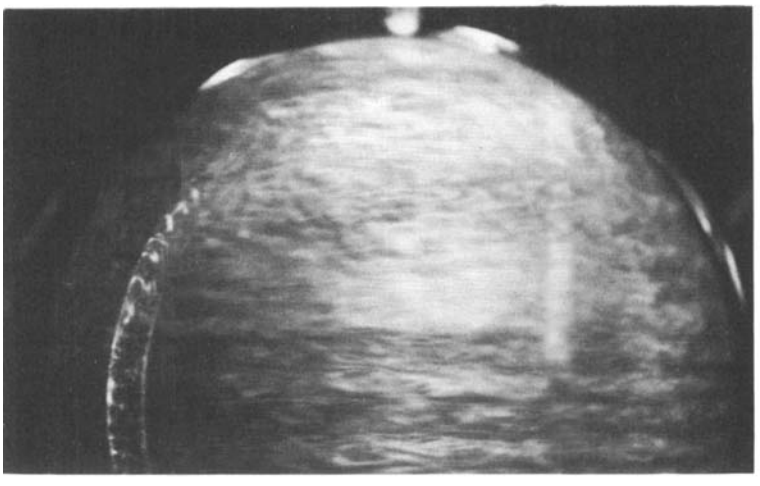

Spiral TG vortices

Rotation

(*d*)

FIGURE 4(*c*, *d*). For caption see facing page.

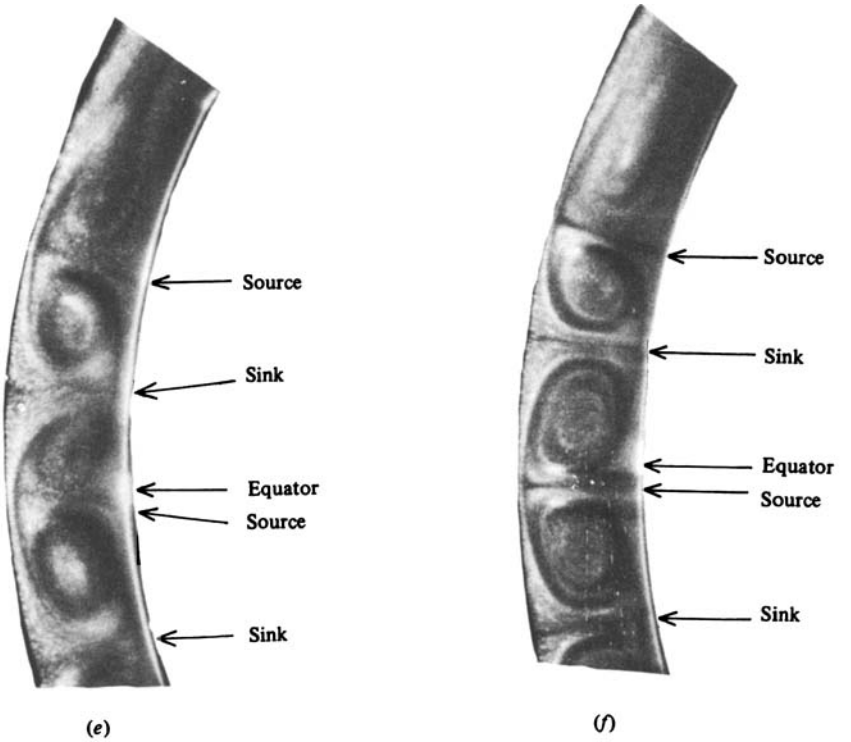


FIGURE 4. Aluminium-flake method. (*a*) Slit-light illumination; II TS, $\beta = 0.024$, $R_e/R_{ec} \approx 1.09$ ($R_e = 1.17 \times 10^4$). (*b*) Front lighting with slit-light illumination; II TS, $\beta = 0.06$, $R_e/R_{ec} \approx 1.18$ ($R_e = 3.247 \times 10^3$). (*c*) Front lighting with slit-light illumination; III WS, $\beta = 0.06$, $R_e/R_{ec} \approx 1.68$ ($R_e = 4.637 \times 10^3$). (*d*) Front lighting with slit-light illumination; IV S, $\beta = 0.06$, $R_e/R_{ec} \approx 1.73$ ($R_e = 4.7749 \times 10^4$). (*e*) Slit-light illumination; III WT, $\beta = 0.138$, $R_e/R_{ec} \approx 4.98$ ($R_e = 4.485 \times 10^3$). (*f*) Slit-light illumination; III T, $\beta = 0.138$, $R_e/R_{ec} \approx 7.61$ ($R_e = 6.846 \times 10^3$).

laminar to turbulent flow. Although the transition process depends on $\beta$, these flow regimes can be generally classified into I, the laminar basic-flow region; II, the TG vortex-flow region including the laminar toroidal and/or spiral TG vortex-flow regimes; III, the transition region including the wavy or periodically and/or unperiodically oscillating TG vortex-flow regimes; and IV, the turbulent-flow region including the chaotic or turbulent TG vortex-flow or the turbulent basic-flow regime. The transition process from the laminar basic-flow region to the turbulent-flow region is shown for each $\beta$ in figure 3. In this study, the flow is evolved by a gradual increase in $R_e$ beyond the critical Reynolds number $R_{ec}$, at which at pair of TG vortices occurs at the equator for each $\beta$.

For $\beta = 0.024$, as $R_e$ increases gradually beyond $R_{ec}$, an array of stable, steady and toroidal TG vortices (Taylor cells) is developed at the equator, and the secondary flow appears near the pole (flow regime II T). When $R_e$ is increased, spiral TG vortices occur on each side of the toroidal TG vortices (flow regime II TS). Figure 4(*a*), obtained by slit illumination, shows a meridian cross-sectional view in the same flow regime. Two stationary cells occur near the equator, and several cells moving towards the pole appear on both sides of the stationary cells on each side of the equator. On the other hand, figure 5 shows an example of oil-film patterns on the rotating inner sphere obtained by the surface oil-flow method in the same flow regime. Ring-shaped (circular) streaks can be seen near the equator, and spiral streaks also are noted on

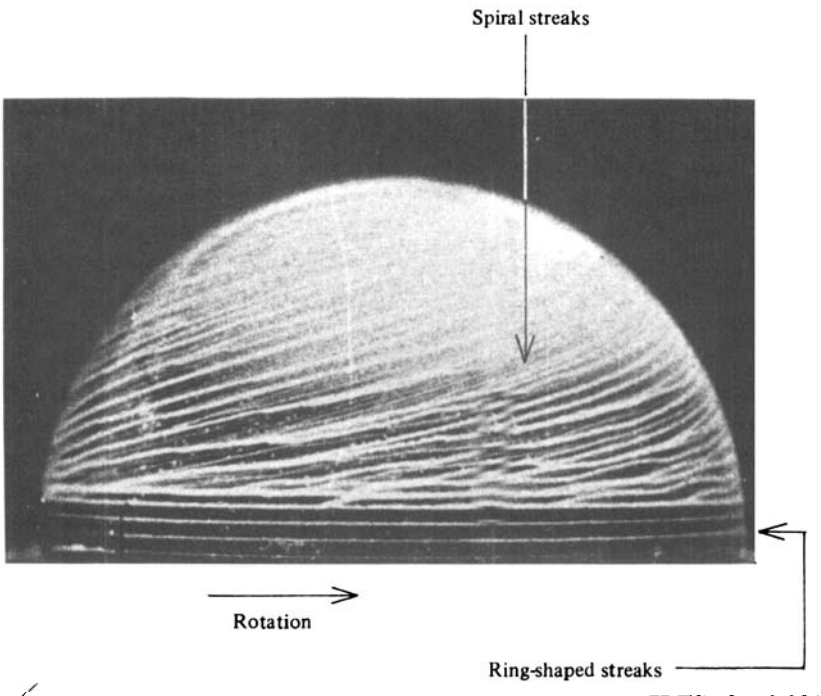


FIGURE 5. Surface oil-flow pattern on the northern hemisphere; II TS, $\beta = 0.024$, $R_e/R_{ec} \approx 1.08$ ($R_e = 1.16 \times 10^4$).

either side of them. The surface oil-flow method is not reliable enough to obtain an accurate flow pattern for small $\beta$. For $\beta \geqslant 0.138$ in this experiment, however, very reliable flow patterns could be obtained. In the present study, the surface oil-flow method was very effective in confirming positive evidence of the occurrence of both toroidal and spiral TG vortices in the same experiment. The combined consideration of both the meridian cross-sectional view and the oil-film pattern revealed that stationary cells near the equator were toroidal, and that moving cells were spiralling. The spatial configuration of these vortices in the spherical annulus will be described in detail below.

With increasing $R_e$, the toroidal TG vortex is absorbed by the spiral TG vortex; then all vortices observed are spiralling (flow regime II S). As $R_e$ is further increased, the spiral TG vortices become wavy, the temporal fluctuations become progressively more complicated, and disturbances in the whole flow appear. With even greater $R_e$, the travelling azimuthal waves superimposed on the spiral TG vortices disappear, but the disturbances in the whole flow remain. The whole flow in the spherical annulus changes gradually to a chaotic one, but a clearly visible structure of spiral TG vortices is still preserved.

For $\beta = 0.06$, the transition process is very similar to that for $\beta = 0.024$, as seen in figure 3. Figure 4(*b*) shows a photograph, taken by slit illumination in addition to front lighting, of the northern hemisphere flow region (flow regime II TS). A pair of vortices located at the equator are understood to be toroidal TG vortices, because they have axes parallel to the equator and are stationary. Vortices which have axes inclined to the equator are spiral TG vortices, because their cells are moving towards the pole. The spatial configuration of the same flow field is schematically drawn in figure 6. When a pair of toroidal cells exists at the equator, as shown in figure 6, the

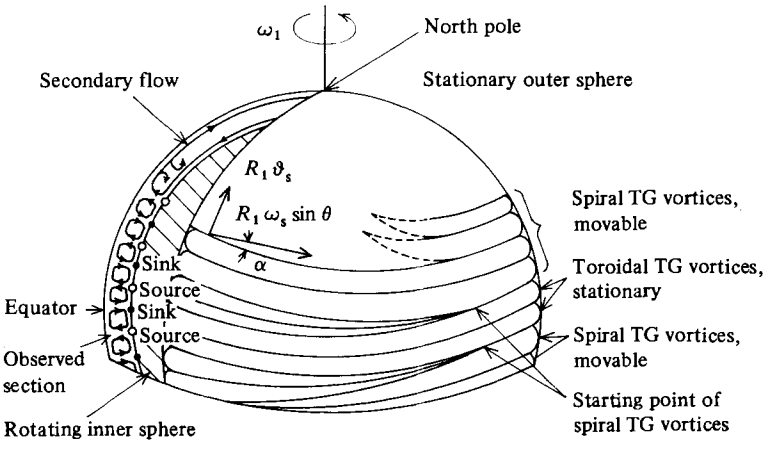


FIGURE 6. Schematic of II TS flow regime; toroidal and spiral Taylor–Görtler vortices and secondary flow.

secondary flow of the cell is directed inwards in the equatorial plane. Consequently, it looks like a sink on the inner sphere. Depending on the direction of the vortex circulation, a sink or source can be presumed to exist on the inner sphere, as described by Sawatzki & Zierep (1970) and Wimmer (1976). Hence the location of toroidal cells can be expressed by stationary sink and source, but the location of spiral cells can be expressed by movable sinks and sources. Starting points of spiral TG vortices are moving in relation to the rotating inner sphere, but in the reverse direction of its rotation, as mentioned below. Tails of spiral TG vortices end in the secondary flow midstream near the pole. Although the appearance of spiral TG vortices was described by Wimmer (1976), no clear spatial configuration of the whole flow field including toroidal and spiral TG vortices nor secondary flow near the pole has been reported. Travelling azimuthal waves on the vortices disappear gradually as $R_e$ increases, and the flow becomes seemingly chaotic. This chaotic flow is shown in figure 4(*d*), where some visible cellular structure is still preserved in spite of the whole turbulent flow field. For still greater $R_e$, the whole flow develops into a turbulent basic flow with no vortex (flow regime IV B).

For $\beta = 0.138$, the flow regimes encountered as $R_e$ is increased from flow regime I B are II T, II TS, III WTS, III WS, III WT and so on, as shown in figure 3. Here both toroidal and spiral wavy-TG vortices can be simultaneously visualized in flow regime III WTS; but, for other $\beta$, the toroidal vortex changes into spiral form at the same time as travelling azimuthal waves occur. Figure 4(*e*) shows the cross-sectional view of toroidal cells immediately after the transition from flow regime III WS into III WT. An oscillation was observed for both sink and source on the inner sphere, but only for the sink on the outer one. With greater $R_e$, the waves disappear and the strong circulation of vortex is remarkably visible on the toroidal cells. A typical cross-sectional photograph of the flow regime III WT is shown in figure 4(*f*). As $R_e$ is increased much further, turbulence appears on the toroidal vortex (flow regime IV T), then a few spiral vortices called Stuart vortices occur in the Ekman boundary layer near the pole (flow regime IV TSt. This Stuart vortex was also reported by Wimmer (1976).

For $\beta = 0.206$, the transition process is very different from other cases. Only a pair of steady toroidal TG vortices occurs (flow regime II T) and no wavy-vortex flow

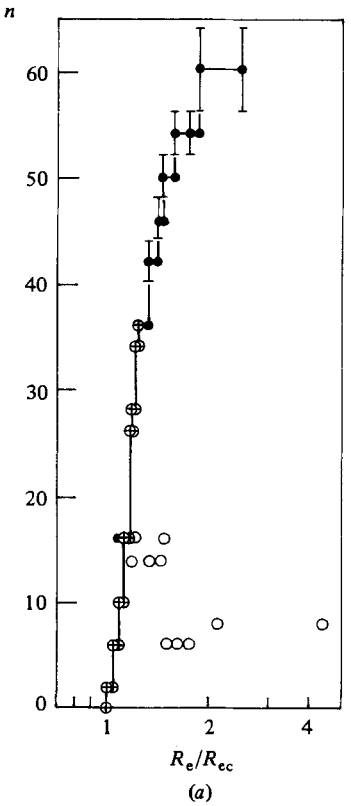


(*a*)

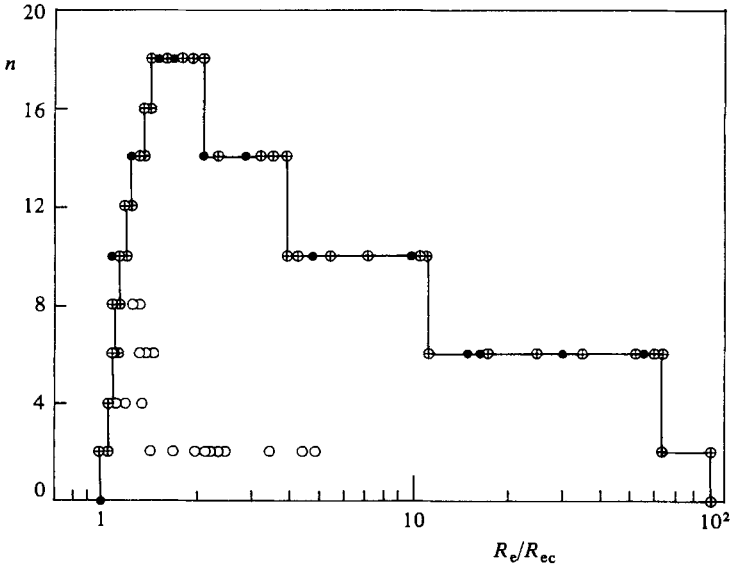


(*b*)

FIGURE 7(*a*, *b*). For caption see facing page.

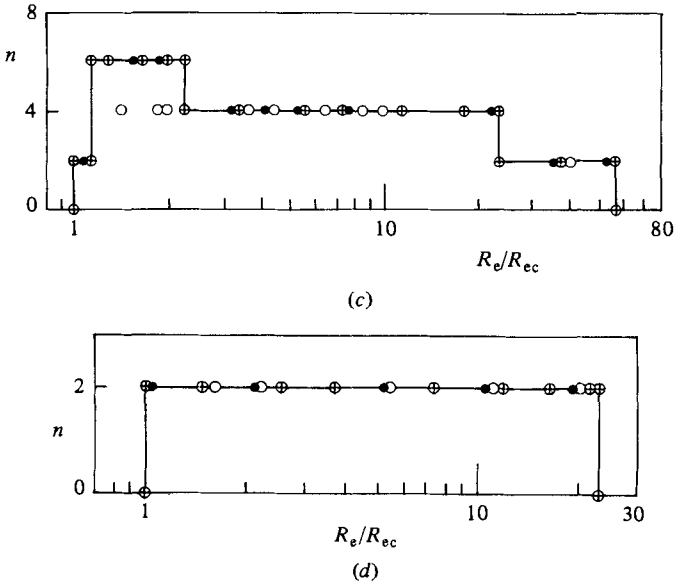


FIGURE 7. Number of Taylor–Görtler vortex cells as a function of $R_e/R_{ec}$ for various $\beta$. ○, Surface oil-flow method; ●, aluminium-flake method by front lighting; ⊕, aluminium-flake method with slit-light illumination: (*a*) $\beta = 0.024$, $R_{ec} = 10700$; (*b*) 0.06, 2760; (*c*) 0.138, 900; (*d*) 0.206, 554.

appears. The Stuart vortex emerges over the great range of $R_e$, i.e. passing through laminar, transition and turbulent regions (flow regimes II TSt, III OTSt and IV TSt).

## 5. Vortex configuration

The TG vortex appears in the form of toroidal and/or spiral cells depending on the flow regimes, as described before. Now, the number of toroidal and/or spiral cells, the location of toroidal cell and the wavelength are discussed as a means to clarify the spatial organization of the vortex.

Figure 7 shows the number $n$ of toroidal and spiral cells as a function of Reynolds number $R_e$ for various values of $\beta$. Data obtained by the surface oil-flow method are compared with those obtained by the aluminium-flake method, not only with front lighting but also with slit-light illumination. Data obtained by the surface oil-flow method are closely dependent on the number of the toroidal cells, because only the ring-shaped (circular) streaks were counted on the generated surface pattern. On the other hand, data obtained by the aluminium-flake method show the total number of both toroidal and spiral cells observed in a meridian cross section. There was no discrepancy among data in terms of the two kinds of illumination techniques employed, either front lighting or slit-light illumination. Data obtained by the surface oil flow have some errors for $\beta = 0.024$ and 0.06 except at around $R_e/R_{ec} = 1$, because the method is not adequate for the case of a great velocity gradient. For $\beta \geqslant 0.138$, however, the toroidal cells could be enumerated correctly by it, and the number was in good agreement with data obtained by the aluminium-flake method, except for the range $R_e/R_{ec} = 1.3$–2.27 of $\beta = 0.138$, where the change from the toroidal to the spiral vortex or vice versa occurred even with a slight perturbation of the flow. Consequently, it is understood that the surface oil-flow method can be correctly used for the gap flow in the case of clearance greater than 10 mm.

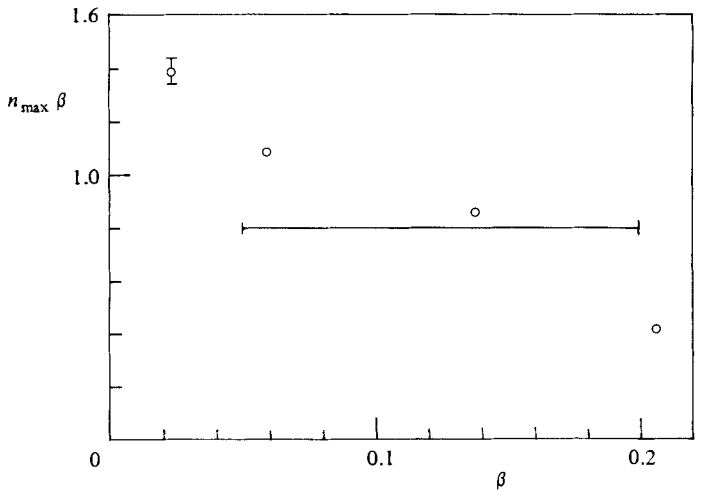


FIGURE 8. Maximum numbers of cells observed at the meridional cross section as a function of $\beta$. ○, present data; ——, Bartels (1978).

For $\beta = 0.024$, the value of $n$ increases rapidly with increasing $R_e$ above $R_e/R_{ec} = 1$. The sharp increase of $n$ is mainly caused by the development of spiral cells, as described below. For $\beta = 0.06$, the value of $n$ increases by 2 with increasing $R_e$, and has a maximum, $n = 18$. Upon further increases of $R_e$, it decreases by four. At $R_e/R_{ec} \approx 90$, no cell appears, and the flow develops into the turbulent basic flow. For $\beta = 0.138$, the maximum $n$ is six, and the value of $n$ is reduced by two with increasing $R_e$. For $\beta = 0.206$, only a pair of toroidal vortices appears over the range $R_e/R_{ec} = 1$–23.

The maximum number of cells $n_{max}$ observed for each $\beta$, as described above, decreases with increasing $\beta$. Bartels (1978) obtained $n_{max} \approx 0.8/\beta$ for $0.05 < \beta < 0.2$ by means of a numerical calculation. Figure 8 shows the value of $n_{max}\beta$ as a function of $\beta$ in a comparison of Bartels' with the present results. For a smaller $\beta$ the present results are greater than Bartels' results, but vice versa for a greater $\beta$.

Figure 9 shows the meridian coordinate $\theta$ (shown in figure 1) of sinks and/or sources of toroidal cells observed on the inner sphere in a meridian cross section of the spherical annulus as a function of $R_e$ for various $\beta$. The solid lines indicated by $\Theta_R$ and $\Theta_D$ show the values of $\theta$ at which a spiral cell breaks and disappears respectively. As shown in figure 6, the tail of the spiral vortex ends in the secondary-flow region near the equator. $\Theta_R$ data were obtained from the measurements of the cell boundary nearest to the pole by slit illumination. On the other hand, $\Theta_D$ data were obtained from the measurements of the location of the tail tip of the spiral vortex by front-lighting observation.

For $\beta = 0.024$, as shown in figure 9 ($a$), a new pair of toroidal cells is added on each side of the pair that occurred at the equator at $R_e/R_{ec} = 1$, when $R_e/R_{ec}$ increases to around 1.04. The pairs of toroidal cells increase with $R_e$, and five pairs appear at $R_e/R_{ec} \approx 1.07$. Upon further increase of $R_e$, the spiral TG vortex occurs at the boundary between the toroidal cell and the secondary flow. Toroidal vortices are gradually absorbed and change into spiral vortices with an increase of $R_e$. At $R_e/R_{ec} \approx 1.12$, no more toroidal cells appear, so the values of $n$, as shown for $R_e/R_{ec} > 1.2$ in figure 7 ($a$), give the number of spiral cells.

For $\beta = 0.06$, a spiral TG vortex occurs first on the northern hemisphere at

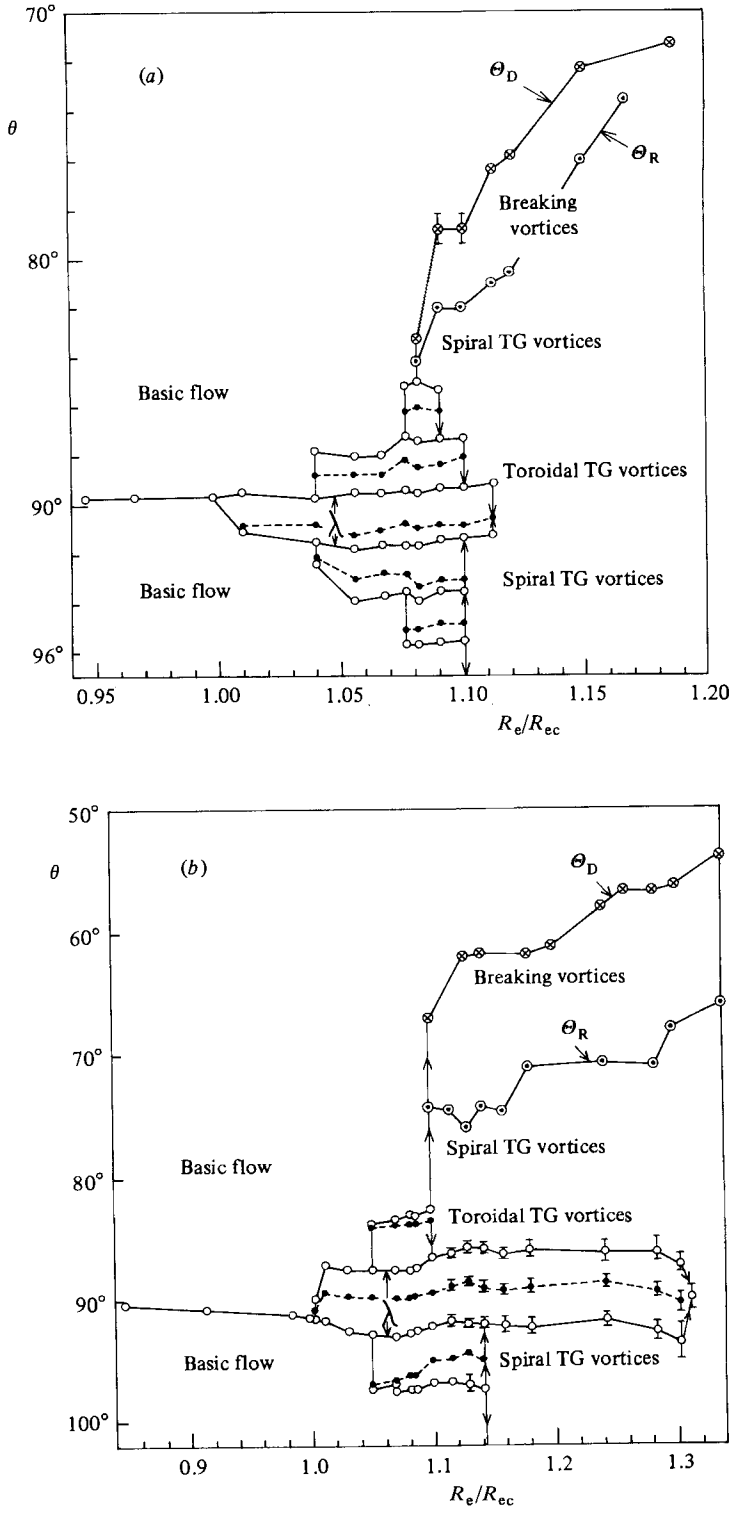


FIGURE 9(*a*, *b*). For caption see p. 224.

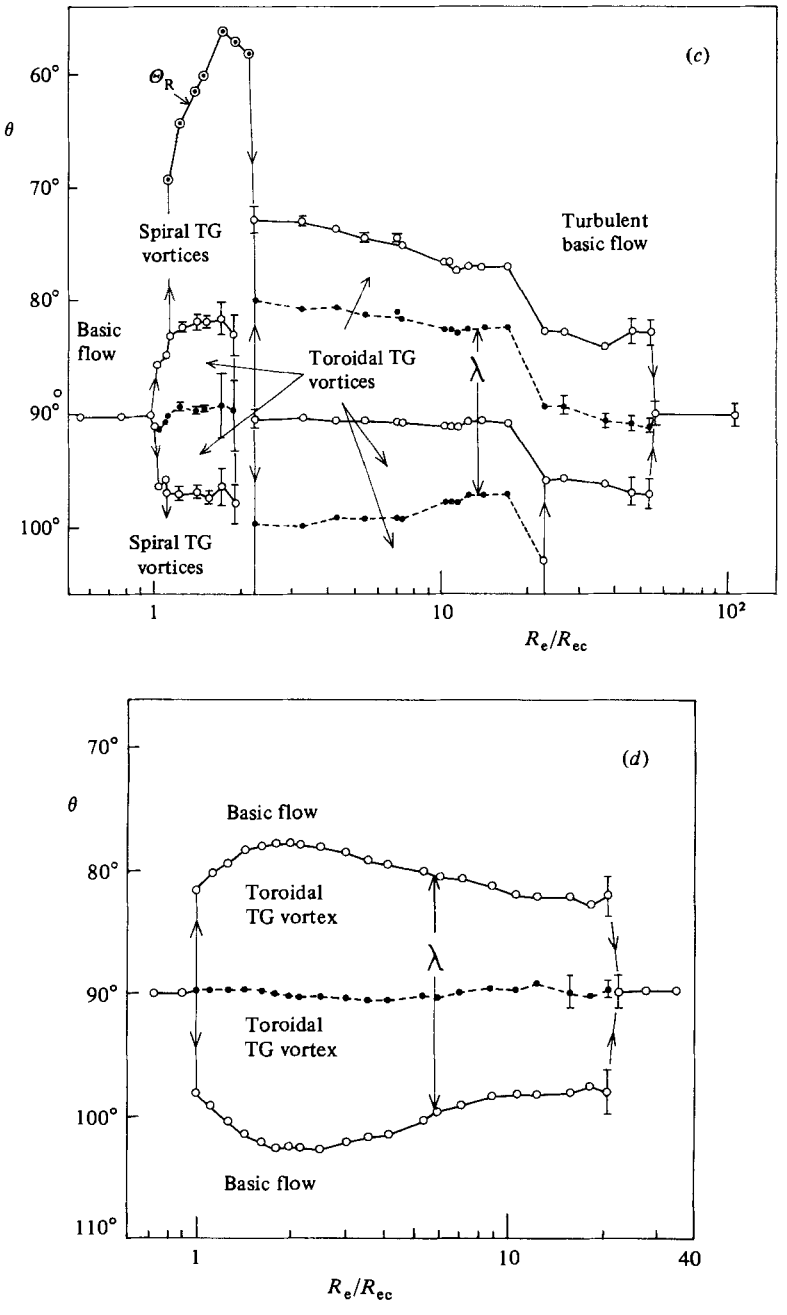


FIGURE 9. Distribution of sources and sinks, and flow regimes for various $\beta$. ○, source; ●, sink. (*a*) $\beta = 0.024$; (*b*) 0.06; (*c*) 0.138; (*d*) 0.206.

$R_e/R_{ec} \approx 1.1$ after the appearance of three pairs of toroidal cells. As soon as the spiral cells occur, the oscillation of the cell boundary appears. The amplitude of the oscillation (indicated by the error bars) increases gradually, as $R_e/R_{ec}$ increases to about 1.3. When $R_e/R_{ec} = 1.31$ is exceeded, no toroidal cell exists.

For $\beta = 0.138$, the spiral vortex occurs on each side of a pair of toroidal cells at the equator, when $R_e/R_{ec}$ increases to 1.13. As soon as the spiral vortex occurs, the

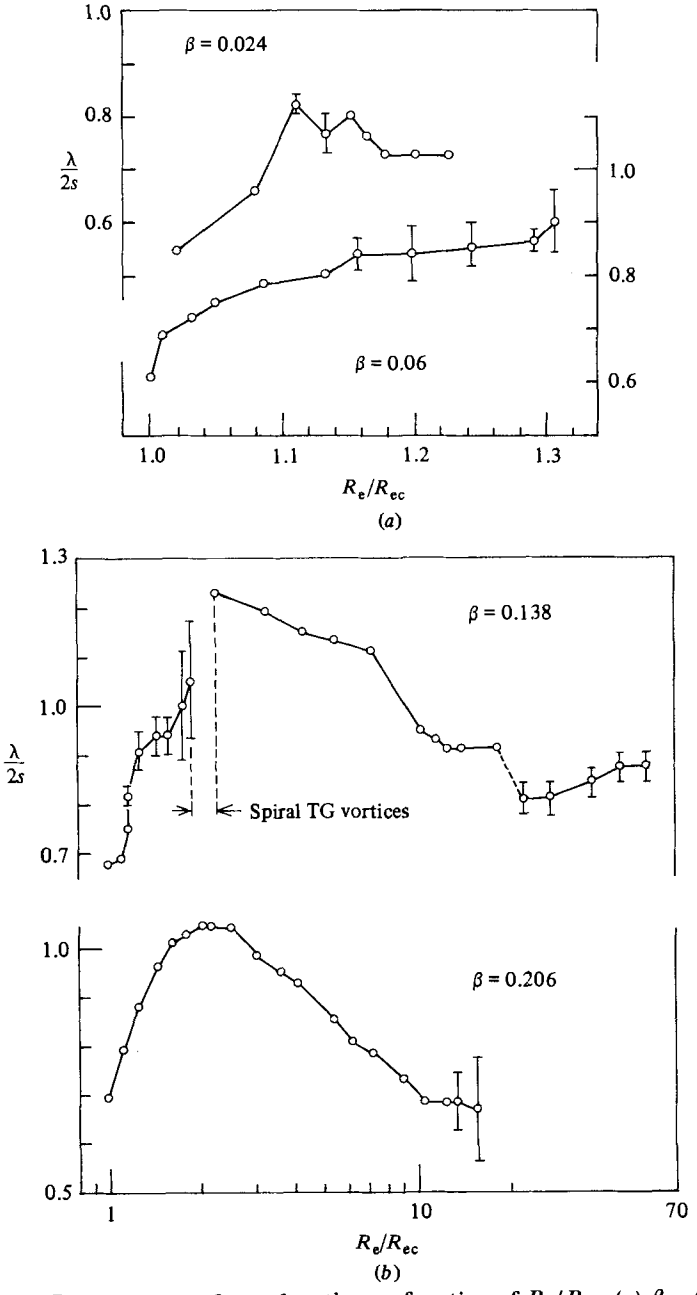


FIGURE 10. Development of wavelength as a function of $R_e/R_{ec}$. (*a*) $\beta = 0.024$ and 0.06; (*b*) 0.138 and 0.206.

cell boundary oscillation (shown by error bars in figure 9*c*) appears. At $R_e/R_{ec} = 1.9$, when the oscillation becomes greatest, the toroidal vortex changes to the spiral vortex. However, when $R_e/R_{ec}$ is increased to around 2.27, all spiral cells suddenly transform again into toroidal cells, so $\Theta_R$ is sharply increased. The oscillation continues over the range $R_e/R_{ec} = 2.27$–7.5, but disappears at $R_e/R_{ec} \approx 7.5$. When $R_e/R_{ec}$ is increased to 17, the toroidal cells move towards the southern hemisphere ($\theta > 90°$), and a pair of them disappears on the southern hemisphere at $R_e/R_{ec} = 23$.

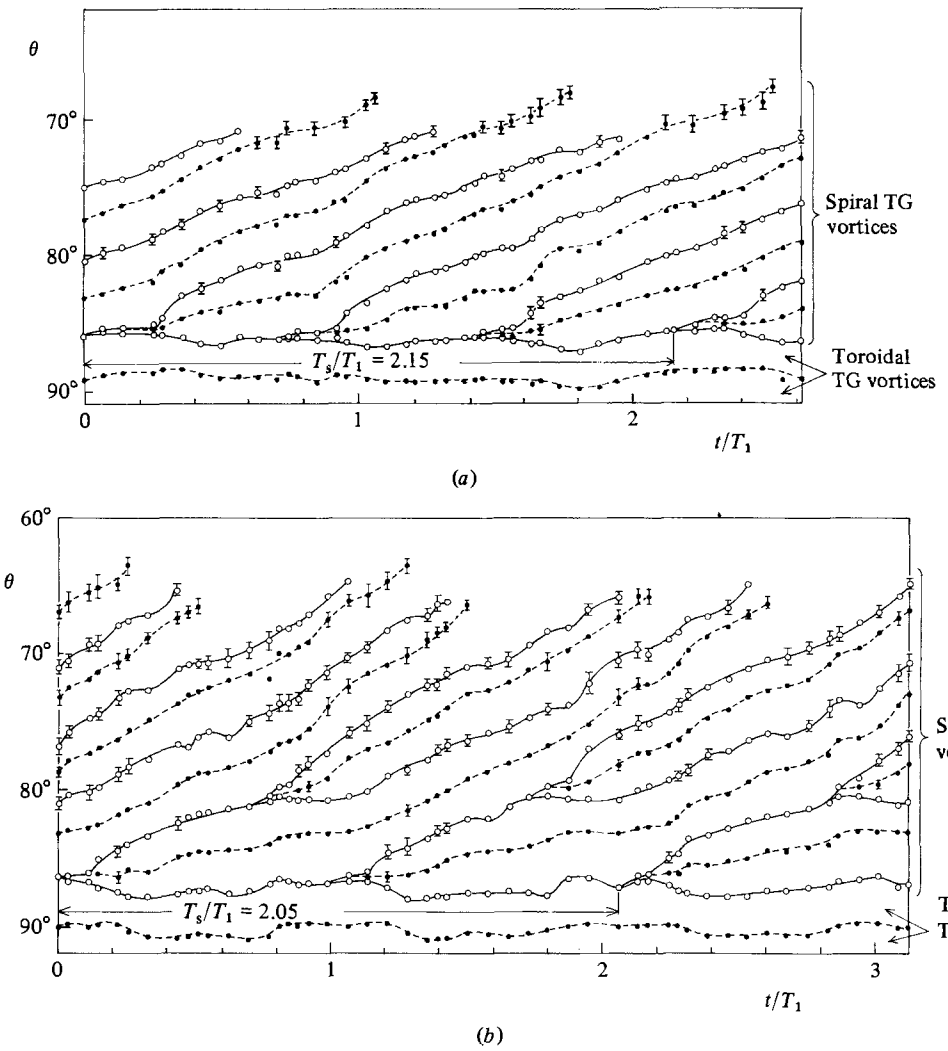


FIGURE 11. Stationary and/or movable sources and sinks for $\beta = 0.06$. ○, source; ●, sink. (*a*) $R_e/R_{ec} \approx 1.2$; (*b*) $R_e/R_{ec} \approx 1.31$.

At $R_e/R_{ec} \approx 48$, the oscillation becomes large again and the whole flow region becomes seemingly chaotic. The toroidal vortex disappears at $R_e/R_{ec} = 59$; the flow then develops into the turbulent basic flow.

For $\beta = 0.206$, as is shown in figure 9(*d*), only a pair of toroidal cells appears. Although the cell-boundary oscillation occurs first on the source at $R_e/R_{ec} = 11$, the oscillation of the sink located at the equator occurs suddenly with a great amplitude at $R_e/R_{ec} = 14$. Then the whole flow region becomes seemingly turbulent, but the pair of the toroidal cells remains. With increasing $R_e$, however, the amplitude of the oscillation increases more and more, and at $R_e/R_{ec} = 23$, the cells disappear at last.

Figures 10 (*a*, *b*) show the relationship between dimensionless half-wavelength $\lambda/2s$ and $R_e/R_{ec}$, where $\lambda$ is the width of a pair of toroidal cells at the equator on the inner sphere and $s$ is the clearance between inner and outer spheres. In the onset phase of the toroidal cells, $\lambda/2s$ increases with $R_e/R_{ec}$. Errors are caused by the oscillation of sink and source for the wavy vortices. For $\beta = 0.138$ the toroidal vortex

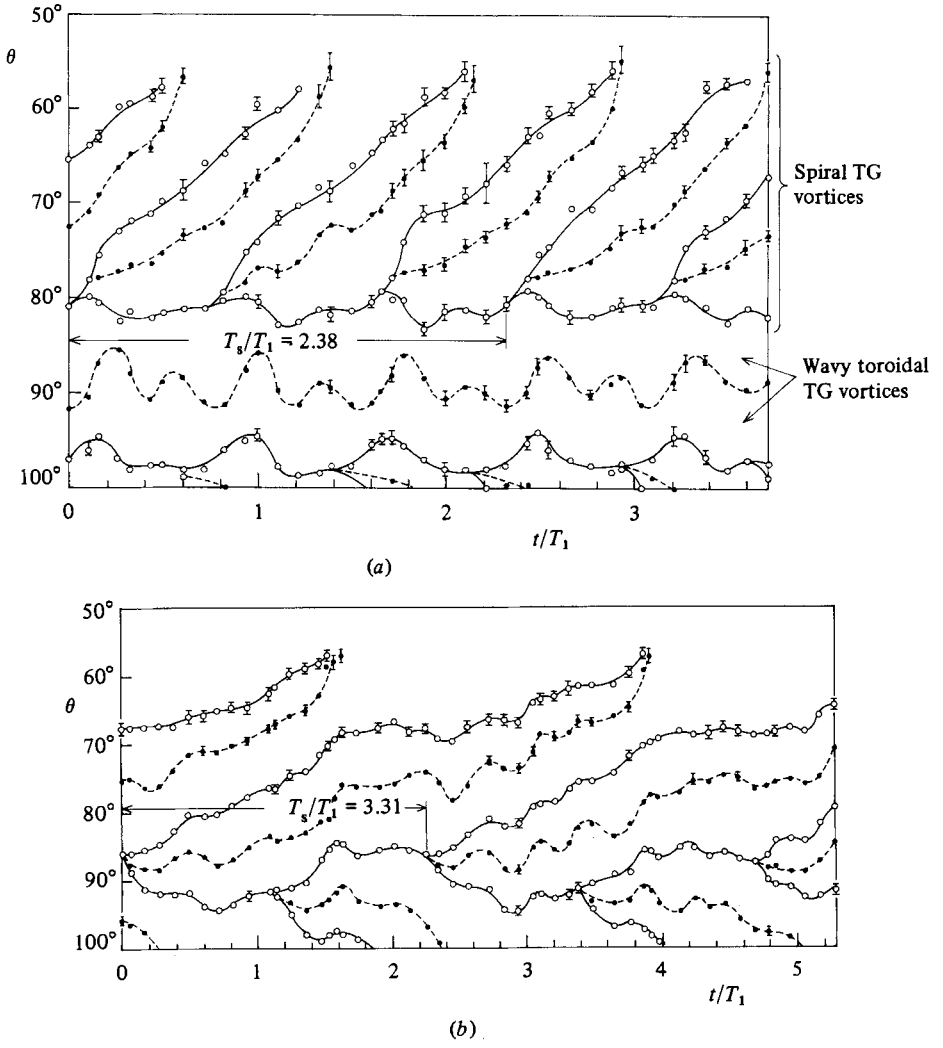


FIGURE 12. Stationary and/or movable sources and sinks for $\beta = 0.138$. ○, source; ●, sink. (*a*) $R_e/R_{ec} \approx 1.78$; (*b*) $R_e/R_{ec} \approx 2$.

disappears at $R_e/R_{ec} = 1.9$, as described above, so that data are not shown in the range of $R_e/R_{ec} = 1.9$–$2.27$. The measured value of $\lambda/2s$ has a maximum value 1.23 at $R_e/R_{ec} = 2.27$, where spiral vortices are suddenly transformed into two pairs of toroidal vortices. Upon further increase of $R_e/R_{ec}$, the value of $\lambda/2s$ decreases. For $\beta = 0.206$, $\lambda/2s$ has a maximum value 1.05 at $R_e/R_{ec} \approx 2$. Wimmer (1976) reported a similar relationship for the dimensionless half-wavelength at $\beta = 0.18$.

In the course of these measurements, the flow modes were obtained only by increasing $R_e$ stepwise. No measurements were done systematically for stepwise-decreasing $R_e$, but a hysteresis phenomenon in the flow modes was found by increasing or decreasing $R_e$ stepwise. In some ranges of $R_e$ for $\beta = 0.024$ and 0.06, incidentally, the position of the cells is not sufficiently symmetric at the equator, as shown in figures 9(*a*, *b*) and 11(*a*, *b*). The symmetry of the flow at the equator could be expected theoretically, but could not be obtained experimentally. It might be due to the driving shaft at the south pole, but this could not be clarified.

| | | | | | | |
|---|---|---|---|---|---|---|
| | | | (a) $\beta = 0.06$ | | | |
| $R_e/R_{ec}$ | 1.14 | 1.16 | 1.2 | 1.25 | 1.29 | 1.31 |
| $(R_e)$ | (3160) | (3210) | (3310) | (3440) | (3570) | (3610) |
| $T_s/T_1$ | 2.15 | 2.14 | 2.15 | 2.15 | 2.15 | 2.05 |
| $\omega_s/\omega_1$ | 0.465 | 0.467 | 0.465 | 0.464 | 0.466 | 0.488 |
| $\omega_s^*/\omega_1$ | −0.535 | −0.533 | −0.535 | −0.536 | −0.534 | −0.512 |
| Number of spiral-vortex starting points | 3 | 3 | 3 | 3 | 3 | 2+2 |
| Number of spiral cells | 6 | 6 | 6 | 6 | 6 | 8 |
| $\theta$ at spiral-vortex starting points | 86° | 86° | 86° | 86° | 85° | 81°<br>86° |
| $\alpha°$, $\theta = 82°$ | 2.2±0.6 | 2.4±0.2 | 2.7±0.2 | 2.6±0.1 | 2.8±0.2 | 2.7±0.5 |
| 78° | 2.6±0.4 | 2.6±0.2 | 2.7±0.2 | 2.7±0.1 | 2.8±0.2 | 3.5±0.3 |
| 74° | 2.9±0.3 | 2.6±0.2 | 2.7±0.2 | 2.7±0.1 | 2.9±0.2 | 3.6±0.3 |
| | | | (b) $\beta = 0.138$ | | | |
| $R_e/R_{ec}$ | 1.27 | 1.57 | 1.78 | 2 | | |
| $(R_e)$ | (1140) | (1410) | (1600) | (1800) | | |
| $T_s/T_1$ | 2.30 | 2.31 | 2.38 | 2.31 | | |
| $\omega_s/\omega_1$ | 0.434 | 0.434 | 0.421 | 0.432 | | |
| $\omega_s^*/\omega_1$ | −0.566 | −0.566 | −0.579 | −0.568 | | |
| Number of spiral-vortex starting points | 3 | 3 | 3 | 1 | | |
| Number of spiral cells | 6 | 6 | 6 | 2 | | |
| $\theta$ at spiral-vortex starting points | 82° | 81° | 81° | 87° | | |
| $\alpha°$, $\theta = 78°$ | 7.6±0.5 | 8.7±0.6 | — | 3.1±0.5 | | |
| 74° | 8.1±0.6 | 9.3±0.9 | 6.4±1.3 | 3.3±0.5 | | |
| 70° | 8.7±0.4 | 10.0±0.9 | 8.5±0.7 | 3.3±0.5 | | |

TABLE 3. Characteristics of spiral Taylor–Görtler vortices

## 6. Structure of the spiral Taylor–Görtler vortex

The spiral TG vortex generally occurs on each side of the toroidal TG vortex located at the equator, as shown in figure 6. The axes of the toroidal TG vortices are parallel to the equator, so the boundaries between them look like stationary sources or sinks in the meridional cross-section of a spherical annulus, as described above. However, the axes of spiral TG vortices are inclined to the equator and rotating, so that the boundaries between them look like movable sources or sinks which are moving towards the pole. Cross-sectional views of these cells were photographed by stroboscopic illumination. The locations of stationary and/or movable sources and sinks were measured from a series of these photographs.

Figures 11 and 12 show the location of sources and sinks as a function of $t/T_1$, where $t$ is the elapsed time and $T_1$ is a period of inner-sphere rotation. At $R_e/R_{ec} \approx 1.2$ (figure 11*a*) the toroidal sink and source are seen to be stationary around a constant value of $\theta$ near $\theta = 90°$ with increasing $t/T_1$, although they fluctuate a little. But the sink and source of the spiral TG vortex change their positions with time. The intersection of two smooth curves, which gradually approach a fixed value (and conjoin movable source and sink data points of spiral cells), with a smooth curve connecting the stationary source data points of toroidal cells at $\theta = 86°$, corresponds to the starting point of the spiral TG vortex shown in figure 6. On the other hand, using front

illumination, the existence of three pairs of spiral TG vortices (i.e. three different starting points on the inner sphere) was confirmed in the flow region of the northern hemisphere. The time $T_s$ required for three starting points to pass the observer, that is the time per spiral TG vortex rotation, was also measured by using a stopwatch to determine visually in real time. Then $T_s/T_1 = 2.15$ was obtained. This value is in good agreement with the value of $T_s/T_1$ that is obtained by measuring the scale of dimensionless time distance from the first intersection (the first starting point) to the fourth intersection (the fourth starting point), as shown in figure 11 (*a*). Hence the angular velocity of the spiral TG vortex $\omega_s$ is obtained as $\omega_s/\omega_1 = T_1/T_s = 0.465$. And its relative angular velocity $\omega_s^*$ in a reference frame that rotates with the inner sphere is also given by $\omega_s^* = \omega_s - \omega_1 = -0.535\omega_1$. The angle $\alpha$ between the axis of the spiral TG vortex and the azimuthal direction is given by

$$\alpha = \arctan[\vartheta_s/\omega_s \sin\theta], \tag{3}$$

where $\vartheta_s$, the angular velocity of the spiral cell in the meridian direction, is given by

$$\vartheta_s = \lim_{\Delta t \to 0} \frac{\Delta\theta}{\Delta t} = \lim_{\Delta t \to 0} \frac{\Delta\theta}{\Delta t/T_1} \frac{1}{2\pi}, \tag{4}$$

where $\Delta\theta$ is the displacement angle of the sink or source in the meridianal cross-section during the elapsed time $\Delta t$. The term $\lim_{\Delta t \to 0} \Delta\theta/(\Delta t/T_1)$ in (4) is calculated from the average gradient of the smooth curve which joins the sink or source in the same figure. Although there is a slight difference in the calculated value depending on $\theta$, $\alpha \approx 3°$ is obtained for $R_e/R_{ec} \approx 1.2$.

For $R_e/R_{ec} \approx 1.31$ (figure 11 *b*), it is remarkable that the spiral vortex can be found at $\theta = 86°$, and that spiral cells also occur at $\theta = 80°$ between two pairs of spiral vortices. Table 3 shows the characteristics of the spiral TG vortex on the northern hemisphere for various values of $R_e/R_{ec}$. The spiral TG vortex rotates at about half the rotation rate of the inner sphere for each $R_e/R_{ec}$, and $\alpha$ increases with a decrease of $\theta$ but an increase of $R_e/R_{ec}$.

Figure 12 shows the same relationship for $\beta = 0.138$. At $R_e/R_{ec} \approx 1{\cdot}27$, a pair of toroidal TG vortices and three pairs of spiral TG vortices appear at the equator and on the northern hemisphere respectively. With increasing $R_e/R_{ec}$, the wave amplitudes of the sink or source curve with both toroidal and spiral cells increase, as seen in figure 12 (*a*). At $R_e/R_{ec} = 2$ (figure 12 *b*), the toroidal cells disappear and the spiral-cell wave amplitudes increase. The number of pairs of spiral vortices is reduced from three to one. Over the range $R_e/R_{ec} = 1.27$–2, $\omega_s$ remains unchanged at about 0.43, as shown in table 3 (*b*); $\alpha$ increases with a decrease of $\theta$ in the same manner as $\beta = 0.06$, but decreases with increasing $R_e$.

This study has been supported by a Grant-in-Aid for Scientific Research from the Ministry of Education of Japan in 1980, and was carried out at the Nagoya Institute of Technology. The author gratefully acknowledges the assistance of Mr Hiroshi Omori in the experiments.

## REFERENCES

Bartels, F. 1982 Taylor vortices between two concentric rotating spheres. *J. Fluid Mech.* **119**, 1.

Bartels, F. 1978 Rotationssymmetrische Strömungen im Spalt konzentrischer Kugeln. Dissertation RWTH Aachen.

KHLEBUTIN, G. H. 1968 Stability of fluid motion between a rotating and stationary concentric sphere. *Fluid Dyn.* **3**, 31.

MUNSON, B. R. & JOSEPH, D. D. 1971*a* Viscous incompressible flow between concentric rotating spheres. Part 1. Basic flow. *J. Fluid Mech.* **49**, 289.

MUNSON, B. K. & JOSEPH, D. D. 1971*b* Viscous impressible flow between concentric rotating spheres. Part 2. Hydrodynamic stability. *J. Fluid Mech.* **49**, 305.

MUNSON, B. R. & MENGUTURK, M. 1975 Viscous incompressible flow between concentric rotating spheres. Part 3. Linear stability and experiments. *J. Fluid Mech.* **69**, 705.

NAKABAYASHI, K. 1978 Frictional moment of flow between two concentric spheres, one of which rotates. *Trans. ASME* I: *J. Fluids Engng* **100**, 97.

NAKABAYASHI, K., YAMADA, Y., MIZUHARA, S. & HIRAOKA, K. 1972 Viscous frictional moment and pressure distribution between eccentric rotating cylinders, when inner cylinder rotates. *Trans. Japan Soc. Mech. Engrs* **38**, 312, 2075.

SAWATZKI, O. & ZIEREP, J. 1970 Das Stromfeld im Spalt zwischen zwei konzentrischen Kugelflächen, von denen die innere rotiert. *Acta Mechanica* **9**, 13.

TAYLOR, G. I. 1923 Stability of a viscous liquid contained between two rotating cylinders. *Phil. Trans. R. Soc. Lond.* **A223**, 289.

VOHR, J. H. 1968 An experimental study of Taylor vortices and turbulence in flow between eccentric rotating cylinders. *Trans. ASME* F: *J. Lubric. Tech.* **90**, 285.

WAKED, A. M. & MUNSON, B. R. 1978 Laminar–turbulent flow in a spherical annulus. *Trans. ASME* I: *J. Fluids Engng* **100**, 281.

WIMMER, M. 1976 Experiments on a viscous fluid flow between concentric rotating spheres. *J. Fluid Mech.* **78**, 317.

YAKUSHIN, V. I. 1970 Stability of the motion of a liquid between two rotating concentric spheres. *Fluid Dyn.* **5**, 660.

YAVORSKAYA, I. M., BELYAEV, YU. N., MONAKHOV, A. A., ASTAFEVA, N. M., SCHERBAKOV, S. A. & VVEDENSKAYA, N. D. 1980 Stability, non-uniqueness and transition to turbulence in the flow between two rotating spheres. *Space Research Institute, Academy of Sciences, USSR.*